Research Paper

3D-CFD investigation into free convection flow above a heated horizontal cylinder: Comparisons with experimental data

Kuang C. Lin [a,*], Yashraj Bhosale [a,b], Cun-Yan Zhou Huang [a]

[a] Department of Mechanical and Electromechanical Engineering, National Sun Yat-Sen University, Kaohsiung 80424, Taiwan
[b] Department of Mechanical Engineering, Indian Institute of Technology, Bombay, Powai, Mumbai 400076, India

HIGHLIGHTS

- A 3D computational model is developed for free convection over a heated cylinder.
- Experimental PIV and *Nu* data are validated by the CFD model for the first time.
- A correlation between the boundary layer and flow mechanisms is revealed.
- Periodic swaying motion in all three dimensions is detected.
- A frequency of Nusselt number variations corresponds to the plume oscillation.

ARTICLE INFO

ABSTRACT

A 3-D computational fluid dynamics (CFD) model is proposed for the first time to predict the existing particle-image velocimetry (PIV) data and measured Nusselt numbers collected from the liquid flow above a heated horizontal cylinder. The simulation results are obtained in the free convective water flow around a heated horizontal cylinder with the top surface open to air in the Rayleigh number range from 10^5 to 5×10^6 and a Prandtl number of 5.98. The submersion depth of the cylinder top below the free water surface is normalized by the cylinder diameter at $H/D = 6$. Excellent agreements between the computed and measured similarity solutions for a Rayleigh number of 1.33×10^6 prove the capability of the computational model to simulate flow velocity, boundary layers and Nusselt numbers present in a vertical plane perpendicular to the cylinder axis at different circumferential locations. The computational results concerning the periodic swaying motion of the plume and its time of a sway period are found to be consistent with the experimental observations. Additionally, the computational analysis reveals the correlation among the near-cylinder flow features, boundary-layer thickness and plume formation region. We further analyze the correspondence between the swaying motion in a plane perpendicular to the cylinder axis and meandering structure coupled with U-shaped velocity profiles in the axial direction. Furthermore, the effect of Rayleigh number on the velocity fields and heat transfer characteristics has been identified. In the frequency spectrum analysis of the Nusselt number fluctuations, we have found the correlation between the oscillation frequency of the plume swaying and heat transfer characteristics.

1. Introduction

Natural convection is widely used as a conventional method for cooling in various applications such as shell tube heat exchangers, electronic cooling, heat transfer through submerged pipelines, steam pipes in power plants and cooler pipes in nuclear reactors. The main advantage of natural convection over forced convection is no need for extra components, which results in high reliability and low costs in design and maintenance.

One of the fundamental problems in natural convection is free convection from a single heated horizontal cylinder submerged in a liquid with a free surface, which has been studied over the past half-century. Several experimental studies have been performed to analyze dynamical behaviors of plumes and heat transfers above a heated cylinder [1–18]. In general, the operational parameters that influence the presence and motion of plumes primarily comprise the Prandtl number, Rayleigh number, submersion depth of the cylinder below the vertically confining surface and magnitude of

* Corresponding author at: 4047 Electromechanical Building, 70 Lien-Hai Rd, Kaohsiung 80424, Taiwan.
  E-mail address: kclin@umich.edu (K.C. Lin).

Nomenclature

Dimensionless variables and numbers

a	coefficients of the discretized governing equations
Gr	Grashof number
Nu	Nusselt number
p	static pressure
Pr	Prandtl number
R^ϕ	residual for dependent variables
R^C	residual for the continuity equation
Ra	Rayleigh number
S	volume-integrated source terms
t	time
T	temperature
V	velocity vectors (u, v, w) in Cartesian coordinates
$\bar{U}$	$(u^2 + v^2 + w^2)^{0.5}$
X	Cartesian coordinates (x, y, z)
ϕ	dependent variables

Dimensional parameters

D	cylinder diameter (m)
g	acceleration due to gravity (m/s^2)
H	submersion depth between the top of the cylinder and the free water surface (m)
k	effective thermal conductivity (W/m/K)
R	cylinder radius (m)
T_c	cylinder surface temperature (°C)
T_o	operating temperature (°C)
T_w	inner wall surface temperature (°C)
V_r	ensemble-averaged radial velocity (m/s)
V_θ	ensemble-averaged tangential velocity (m/s)
$\bar{V}_r$	time-series-averaged radial velocity (m/s)
$\bar{V}_\theta$	time-series-averaged tangential velocity (m/s)

α	thermal diffusivity (m^2/s)
β	thermal expansion coefficient (1/K)
$\bar{\delta}$	boundary-layer thickness (m)
ρ	density (kg/m^3)
μ	dynamic viscosity (kg/m/s)
ν	kinematic viscosity (m^2/s)

Math symbols and coordinates

∇	gradient operator $[\partial/\partial x, \partial/\partial y, \partial/\partial z]$
x, y, z	Cartesian coordinates
r, θ, z	cylindrical coordinates
η	boundary-layer radial coordinate

Superscripts

$\prime$	dimensional scale
$*$	dimensionless scales in the radial direction for similarity solutions
$**$	dimensionless scales in the radial direction for general solutions

Subscripts

c	cylinder
f	film quantity
max	maximum
nb	neighboring nodes
P	center nodes
r	radial quantity
w	wall
0	starting time of a sway period
θ	circumferential quantity

---

horizontal confinement. If the cylinder top is too far or too close from the free liquid surface, periodic motion of plumes ends [10,15]. In particular, laminar plumes are usually seen at a Rayleigh number in the order of magnitude of 10^6 and turbulent plumes can be observed at a Rayleigh number approximately higher than 10^7.

In terms of experiments, various phenomena have been observed, including plume swaying motion in a plane perpendicular to the cylinder axis [1–9,12,15], plume meandering motion in a horizontal plane above the cylinder [2,4,5,7,15], turbulent transition [9,12], turbulent plumes [9,12], and U-shape features between two closely spaced narrow plume regions [15]. In addition, measurements were performed, including frequency of swaying motion [2,7,12,15,16], wavelength of meandering motion [7,15], flow velocity [8,10,12,13,15,16], flow temperature [1,6,9,10], flow boundary-layer thickness [16] and Nusselt numbers (Nu) [10,11,13,14]. Specifically, the correlation between the frequency of the swaying motion and wavelength of the meandering motion has been identified [7,15]. In the recent particle-image velocimetry (PIV) measurements [15], the vortex dynamics was found to be correlated with the plume swaying and meandering. From the outcomes of experimental investigations, it has been known that heat and fluid flow above a horizontal cylinder can be unsteady and act in a three-dimensional space.

Several theoretical and analytical studies were first carried out in 1960–1970s to investigate free convection flows around a cross-section of a single cylinder. These studies include empirical correlation equations for estimating area and time-averaged Nusselt numbers [19,20], boundary layer solutions near the cylindrical surface [21], and mathematical solutions for 2-D velocity and temper-

ature distributions in steady laminar plumes [4,17,22–25]. Furthermore, various numerical models have been proposed to simulate external natural convection flows from one or multiple horizontal isothermal cylinders with the help of computational fluid dynamics (CFD). In early CFD studies concerning a single cylinder submerged in flows, computational models were developed using steady-state momentum and energy equations in 2-D cylindrical coordinates [26–28] and Cartesian coordinates [29]. Typically, the proposed analytical and computational models were validated against experimentally measured data for time-series-averaged Nu distributions on a cylinder surface or isotherms of a steady plume. It should be noted that these computed plume structures perpendicular to the cylinder axis are always centralized due to a steady-state condition at a Rayleigh number <10^6 used. Later, transient natural convection was considered in a 2-D computational analysis to capture plume growth and predict plume swaying above a heated cylinder [18]. Besides, 2-D CFD models for nature convection flows above a single cylinder were also analyzed in different studies that investigated the effect of multiple heated cylinder on heat transfer performance in steady-state [30–33] or unsteady-state fluid flows [34]. Most recently, a 3-D CFD transient model was proposed to study the effect of inclination of condenser tubes on natural convection [35]. The authors analyzed the transient variations of the water temperature and average heat transfer coefficients. Overall, our review implies the need for the development of 3-D CFD transient models toward the comprehensive analysis of heat and fluid flows above a heated cylinder.

Although the most recent PIV measurements have discovered the effect of plume motion on the boundary layer, plume formation

region and surrounding flow fields [15,16], there are no computational models of fluid dynamics available in the literature that have demonstrated the mechanism of this free convective flow phenomenon. Prompted by this consideration, in this research, a 3-D CFD model based on the finite volume method is proposed for the first time to predict the experimentally measured flow features that govern the heat transfer characteristics in this commonly applied device.

2. Methodology

2.1. Physical model

The computational model follows exactly the experimental setup used in the studies of Kuehner et al. [15,16]. Fig. 1 shows the 3-D computational domain consisting of a heated cylinder placed in a square-based tank filled with water, where the origin of the Cartesian coordinate system is located on the top surface of the cylinder and the z axis lies along the axial position of the cylinder. The liquid volume has a square base of 0.6 m by 0.6 m and a height of 0.7651 m. The cylinder with an outer diameter of D = 25.4 mm is located approximately at the geometric centre of the tank. H is the submersion depth of the cylinder below the vertically confining surface. We fix H/D = 6 throughout the study for comparing the presence of plume swaying and meandering reported in the experiments.

Based on Refs. [15,16], the setup is chosen to eliminate the effects of horizontal confinement on the results obtained in the fluid flow. No-slip and isothermal boundary conditions are imposed at the walls of the tank and cylinder. Referring to the study of Marjang [36], a symmetry boundary with no velocity gradient in the y-direction is used for the free water surface. The outer surface of the cylinder and inner surface of the tank walls are maintained at constant temperatures of T_c = 301 K and T_w = 297 K, respectively. Fluid motion is induced by the buoyancy force with the temperature difference between the cold fluid and cylinder surface.

2.2. Governing equations

The mathematical equations describing the physical model are based on the assumptions that (i) the fluid thermophysical properties are constant except for the density in the buoyancy force; (ii) the Boussinesq approximation is reasonably accurate for the buoyancy terms in the momentum equations due to the small density variation; (iii) fluid is Newtonian, incompressible and laminar, and (IV) the radiation heat transfer between the wall and cylinder is negligible when compared with the mode of heat convection.

To obtain the dimensionless form of the governing equations, all the dimensional variables identified by a prime are nondimensionalized using the following parameters:

$$t = \frac{\alpha t'}{D^2}, \; X = \frac{X'}{D}, \; V = \frac{V'}{\alpha/D}, \; T = \frac{T' - T_f}{T_c - T_w}, \; p = \frac{p'}{\rho(\alpha/D)^2},$$

$$Ra = \frac{g\beta(T_c - T_w)D^3}{\nu\alpha}, \; Pr = \frac{\nu}{\alpha},$$

$$Gr = \frac{g\beta(T_c - T_w)D^3}{\nu^2} \tag{1}$$

where t, X, V, T and p, respectively, represent the time, Cartesian coordinates (x, y, z), velocity vector (u, v, w), temperature and pressure. In Eq. (1), the thermal diffusivity (α), density (ρ), kinematic viscosity (ν) and thermal expansion coefficient (β) are calculated at the film temperature of T_f = 299 K. g in the Ra and Gr numbers is the gravity. The Prandtl number, Pr, is fixed at 5.98, while the Grashof number, Gr, is given by Ra/Pr.

For the predictions of radial and tangential velocities, a cylindrical coordinate system (r, θ, z) is chosen with its origin at the top edge of the cylinder (see Fig. 1). The tangential coordinate θ is 0° at the bottom of the cylinder and increases clockwise. We introduce two sets of nondimensional physical quantities in the cylindrical coordinate system. The first set is able to yield similarity solutions independent of the Grashof number:

$$\eta^* = Gr^{0.25}\frac{r' - R}{R}, \; V_r^* = \frac{RV_r'}{\nu Gr^{1/4}}, \; V_\theta^* = \frac{RV_\theta'}{\nu Gr^{1/2}}, \; \bar{\delta}^* = Gr^{1/4}\frac{\bar{\delta}'}{R} \tag{2}$$

where η^*, V_r^*, V_θ^* and $\bar{\delta}^*$ are the boundary-layer radial coordinate, ensemble-averaged radial velocity, ensemble-averaged tangential velocity and boundary layer, respectively. R is the cylinder radius. The scaled parameters in Eq. (2) are used in Section 3.1 for comparing computational and experimental results. The second set of the
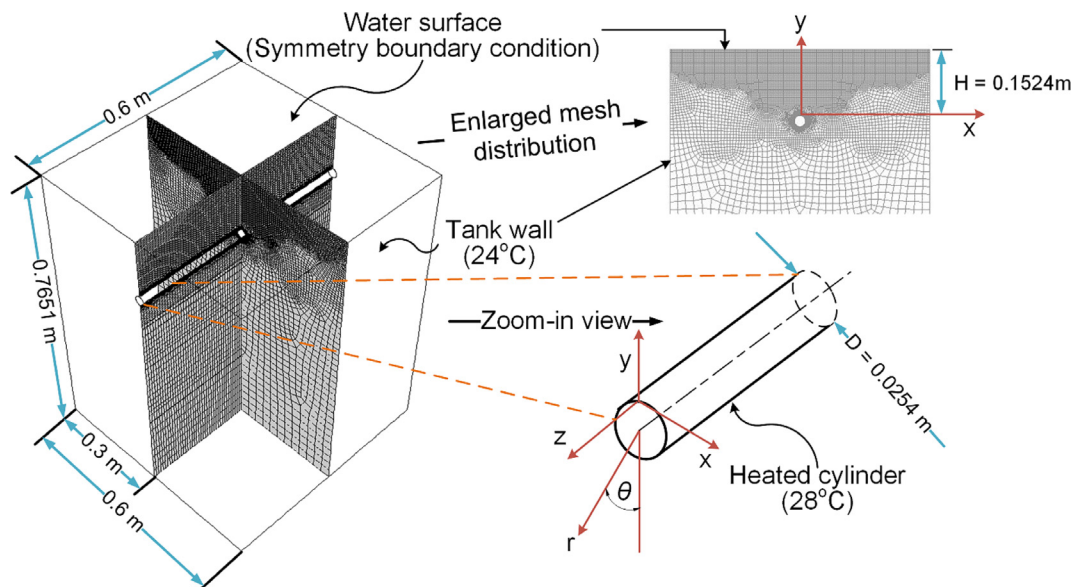

Fig. 1. Schematic of the physical model and mesh used in this study.

dimensionless physical quantity is employed for the Grashof-number-dependent solutions:

$$\eta^{**} = \frac{r'-R}{R}, \quad V_r^{**} = \frac{RV_r'}{v}, \quad V_\theta^{**} = \frac{RV_\theta'}{v}, \quad \delta^{**} = \frac{\delta'}{R} \tag{3}$$

These scaled parameters in Eq. (3) are used in Section 3.3 for analyzing the Rayleigh number effect on the fluid dynamics.

The 3-D dimensionless equations for the conservation of the total mass, momentum and energy of the fluid can be written as:

Continuity equation:

$$\nabla \cdot V = 0 \tag{4}$$

Momentum equation:

$$\frac{\partial V}{\partial t} + (V \cdot \nabla)V = -\nabla p + Pr\left(\nabla^2 V\right) + F_y \tag{5}$$

Energy equation:

$$\frac{\partial T}{\partial t} + V \cdot \nabla T = \nabla^2 T \tag{6}$$

where ∇ represents the gradient operator $[\partial/\partial x, \partial/\partial y, \partial/\partial z]$. $F_y = Ra \cdot Pr \cdot T$ in Eq. (5) only acts on the y-component of the velocity.

The heat transfer characteristics are evaluated by the axially-averaged local Nusselt number of the fluid at the cylinder surface,

$$Nu(t, \theta) = \frac{\partial T}{\partial r} \tag{7}$$

where the radial coordinate r is nondimensionalized by the cylinder diameter. Temperature monitoring points are placed along the cylinder length at different circumferential locations (θ). The Nu number is expected to depend on a number of factors such as the Pr number, Ra number and submersion depth (H/D). By integrating the axially-averaged local Nu number, the time-averaged Nu number can be derived by:

$$\overline{Nu}(\theta) = \frac{1}{t_p} \int_0^{t_p} Nu(t, \theta)dt \tag{8}$$

where t_p in Eq. (8) is the dimensionless acquisition time of 0.3429, which corresponds to 1500 s.

2.3. Numerical methods and validation

We employ Gambit v2.3.16 [37] and ANSYS Fluent v16.1 [38] for mesh generation and solving the heat convection equations, respectively. The 3-D conservation Eqs. (3)–(5) are discretized with the QUICK scheme and solved by means of an implicit finite volume scheme based on the iterative SIMPLE algorithm employed for pressure-velocity coupling. After discretization, the dependent variables (ϕ), including velocity and temperature at each grid cell P, are calculated by:

$$a_P\phi_P = \sum_{nb} a_{nb}\phi_{nb} + S \tag{9}$$

where a_P and a_{nb} are the coefficients of the center and neighboring nodes, respectively. S in Eq. (9) represents the volume-integrated source term in the momentum equation. The imbalance in Eq. (9) summed over all cells P in the computational domain is gauged by the globally scaled residual (R^ϕ):

$$R^\phi = \left(\sum_{\text{all cells}} \left|\sum_{nb} a_{nb}\phi_{nb} + S - a_P\phi_P\right|\right) / \left(\sum_{\text{all cells}} |a_P\phi_P|\right) \tag{10}$$

For the continuity equation, the unscaled residual for the pressure-based solver is defined as:

$$R^C = \sum_{\text{all cells}} |\text{Rate of mass creation in each cell } P| \tag{11}$$

The globally scaled residual is defined as R^C in the last iteration, divided by the largest R^C presented in the first five iterations. In the present simulation, the scaled residuals of the continuity and momentum are set to be 10^{-4} for the convergence criterion, while the residual of energy is set to less than 10^{-6}.

With regard to the mesh generation, we make 120 grids along the cylinder perimeter and 16 boundary layers around the cylinder surface. The grid independence is reached on a total nonuniform hexahedral cells number of 954,800 with more nodes accumulated in the region of plume formation and swaying (see Fig. 1). Then, the pseudo steady-state solutions for the velocity and temperature fields are used to serve as the initial conditions to speed up the transient simulation. After the volume-weighted average temperature reaches a constant value, we define $t = 0$ as the inception of the periodic steady-state behavior of the convective flow.

In addition to the grid independent test, the validity of the computational model is assessed by the time step independence with three different time step sizes, $\Delta t = 5.715 \times 10^{-5}$, 1.143×10^{-4} and 1.715×10^{-4}. Fig. 2 shows the prediction errors introduced by varying the time step size for the time-series-averaged circumferential ($\bar{V}_r'$) and tangential ($\bar{V}_\theta^*$) velocities at $\theta = 90°$. These ensemble averaged velocity data are time-averaged over the acquisition time of 0.3429 (1500 s) in the periodic steady-state solutions. It is seen that the error percentages of $\bar{V}_r'$ and $\bar{V}_\theta^*$ are well below 2% when the time step size Δt is increased from 1.143×10^{-4} to 1.715×10^{-4} or decreased from 1.143×10^{-4} to 5.715×10^{-5}. Accordingly, $\Delta t = 1.14 \times 10^{-4}$ corresponding to the dimensional time step size of 0.5 s is chosen to calculate the flow and heat transfer behavior in this study.

3. Results and discussion

3.1. Comparison with measured velocity fields

Fig. 3 compares the present simulation, analytical solutions [23] and experimental results [16] at $Ra = 1.33 \times 10^6$ for the time-series-averaged radial ($\bar{V}_r^*$) and tangential ($\bar{V}_\theta^*$) velocity profiles in the xy-plane. The data documented are clockwise from the bottom to the top of the cylinder. These velocity profiles provide a deep insight into how the boundary layer merges with the plume. It is seen that the computed velocity profiles accurately predict the experimental data obtained from different angular positions
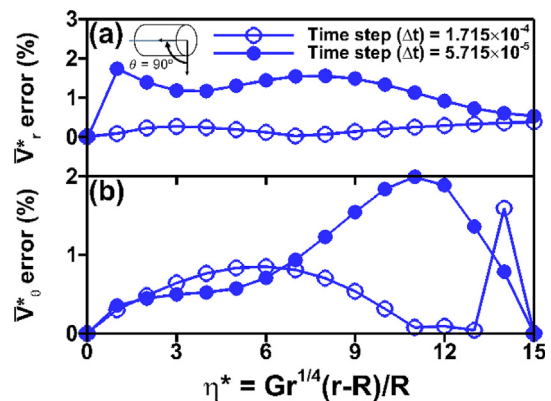

Fig. 2. Sensitivity test for the time-step independence using errors of ensemble-averaged radial ($\bar{V}_r^*$) and tangential ($\bar{V}_\theta^*$) velocities relative to the results with a time step size of $\Delta t = 1.143 \times 10^{-4}$. The velocity data are documented at a circumferential location of 90 degrees. $\Delta t = 5.715 \times 10^{-5}$, 1.143×10^{-4} and 1.715×10^{-4} correspond to 0.25 s, 0.5 s and 0.75 s in dimensional time, respectively.
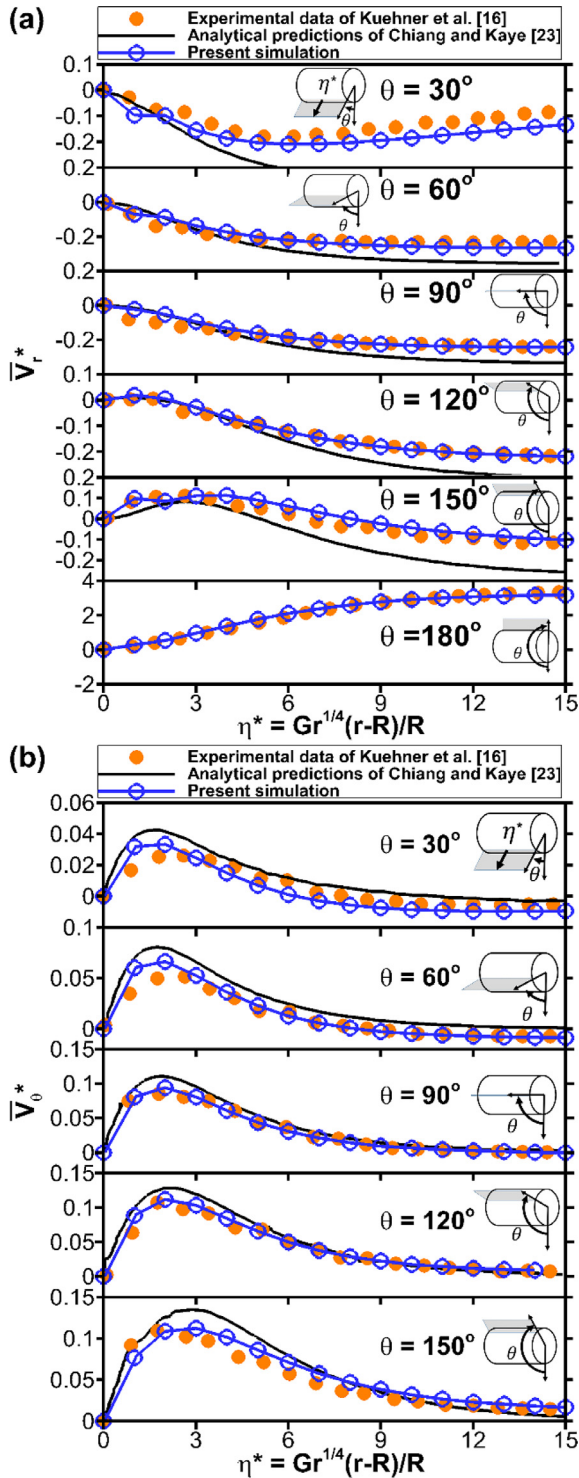
Fig. 3. Time- and z-averaged dimensionless velocities in the yz-plan at various circumferential positions (θ) along the radial direction (gray regions): (a) radial ($\bar{V}_r^*$) velocity and (b) tangential ($\bar{V}_\theta^*$) velocity. Note that $\bar{V}_\theta^*$ at $\theta = 180°$ is unavailable in the analytical solutions. The acquisition time of 0.3429 (1500 s) is used.

The computed time-series-averaged radial ($\bar{V}_r^*$) and tangential ($\bar{V}_\theta^*$) velocities within and just outside the boundary layer also verify the experimental analysis discussed by Kuehner et al. [16]. As shown in Fig. 3a, negative $\bar{V}_r^*$ values that indicate the approach flow moving inward to the cylinder are seen within the boundary layer ($\eta^* < 12$) at $30° \leq \theta \leq 120°$ and just outside the boundary layer at $30° \leq \theta \leq 150°$. Besides, the positive values of $\bar{V}_r^*$ at $150° \leq \theta \leq 180°$ are indicative of rapid boundary layer growth as seen in the later discussion and the fact that the boundary layer finally merges into the plume at the top of the cylinder. At $\theta = 180°$, where the fluid moves away upward from the cylinder top and enters the plume formation region, the radial velocity values ($\bar{V}_r^*$) are constantly positive and of larger magnitude than those at the other degrees. Furthermore, toward the top of the cylinder near the plume formation region, the boundary layer moves away from the heated cylinder wall into the flow. As shown in Fig. 3b, $\bar{V}_\theta^*$ values, which are always positive in the range of $30° \leq \theta \leq 180°$, increase radially outward from the cylinder surface to achieve a maximum at $\eta^* \approx 2$–3 and subsequently decrease to the level of the approach flow at the boundary layer. In addition, the maximum value of $\bar{V}_\theta^*$ obtained at each angular position (θ) increases circumferentially from the bottom to the top of the cylinder, indicating the enlarged circumferential momentum in the boundary layer.

Following the method introduced by Kuehner et al. [16], we identify the boundary-layer thickness which is defined by 12% of the local maximum tangential velocity ($\bar{V}_\theta^*$) in the boundary-layer coordinate along $0 \leq \eta^* \leq 15$ at each angular position (see Fig. 4a). Similar to what was reported by Kuehner et al. [16], the time-averaged thickness of boundary layers ($\bar{\delta}^*$) is able to be established in the circumferential range of $30° \leq \theta \leq 150°$ (see Fig. 4b). It is seen in Fig. 4 that these comparisons show very good agreements between the present simulations and previous experimental results. The $\bar{V}_{\theta,max}^*$ value increases from $\theta = 30°$ until reaching $\theta = 120°$, where the plume formation region begins. With regard to the growth of the boudnary layer thickness around the cylinder, the rapid rise is seen at $\theta = 90$–150° in Fig. 4b, which corresponds to the outward shift of $\bar{V}_\theta^*$ peaks from $\theta = 90$–150° in Fig. 3b. The correlation between the boundary-layer thickness and heat transfer characteristics will be discussed in Section 3.4.
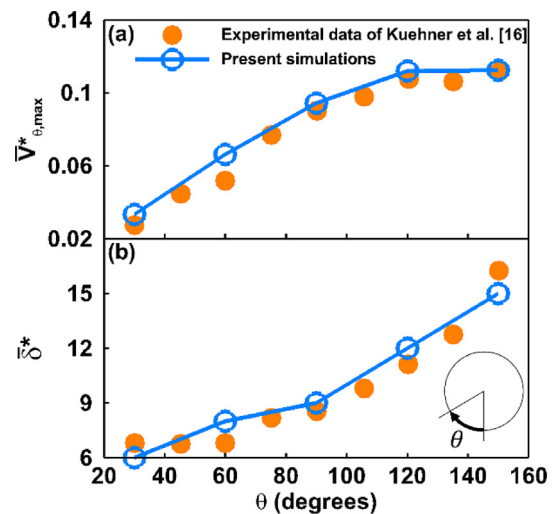

Fig. 4. Variations of the maximum time-averaged tangential velocity ($\bar{V}_\theta^*$) (a) and time-averaged boundary-layer thickness ($\bar{\delta}^*$) (b) with various circumferential positions (θ).

within the boundary layer except for the locations of $\eta^* = 1$–2 where $\bar{V}_\theta^*$ values at $\theta = 30°$ and 60° near the cylinder surface are slightly overpredicted. In general, the computed values are in better agreement with the experimental data than the analytical solutions. For all the angular positions analyzed, the analytical solutions consistently underpredict the experimental $\bar{V}_r^*$ values at $\eta^* > 4$ and overpredict the measured peaks of $\bar{V}_\theta^*$ values.

Fig. 5 shows the time-dependent change of the ensemble-averaged tangential velocity (V_θ^*) and radial velocities (V_r^*) at the angular position $\theta = 90°$. In general, both V_θ^* and V_r^* continuously oscillate in the periodic steady-state. Particularly, the oscillation of V_r^* is relatively pronounced outside the boundary layer, indicating the influence of the plume motion on the approach flow. This observation, however, is not notably shown in V_θ^* which degree of oscillation is quite consistently present along the radial direction.

3.2. Plume formation characteristics

In our simulation results, the computed mechanism of the fluid convection is found to agree reasonably well with the experimental observation by Kuehner et al. [15]. The heated fluid rises along the cylinder surface and separates from the angular positions around 150 to 180 degrees which is known as the plume formation region. The heated fluid then rises through the plume due to the buoyant force and further reaches the free water surface in which the fluid momentum is transported into the horizontal xz-plane. The horizontally moving fluid called a plume mixing layer cools down along the horizontal surface and eventually mixes with the quiescent fluid.

Fig. 6 presents the comparison of the computed velocity fields and the experimentally observed plume centerline from Kuehner et al. [15]. These computed results appear to be in qualitative agreement with the features of the temporal dynamics of the plume. From Fig. 6a and b, the plume that starts swaying to the left moves toward the middle of the xy-plane. The motion of vortices near the plume is seen in Fig. 6b.1. In Fig. 6c, the plume crosses the middle of the xy-plane and vortices shift outward. In Fig. 6d, the plume starts to tilt back toward the right side of the xy-plane. Comparing the dimensionless time interval between 0.01 in Fig. 6a, b and 0.004 in Fig. 6c and d, the predicted plume motion

tends to reside on one side of the axial centerline plane longer than the other. This tendency supports and is consistent with the experimental observation [15]. In Fig. 6d, the vortex is seen to form on the lower side of the plume, which agrees with the position of $y/H = 0.5$ observed by Kuehner et al. [15].

A more detailed insight into the correlation between the velocity and temperature fields for a cycle is presented in Fig. 7. The dimensionless cycle time corresponds to 180 s observed by Kuehner et al. [15]. As can be seen from the correspondence between the momentum and energy transports, temperature-induced buoyant convection near the surface of the heated cylinder constitutes the momentum of the plume that advects the flow temperature. The presence of a mushroom-shaped plume head, seen in Fig. 7c, e and f, correlates with the location where vortices form alongside of the plume. We also can clearly see that a depth of the thermal-mixing zone corresponds to the size of a vortex zone.

Fig. 8 presents time-series averaged velocity and temperature profiles as observed in the xy- and xz-planes at different locations of z/D and y/D, respectively. As seen from above, the flow appears to be a meandering sine wave which appears to travel in the negative z direction. The meandering convex curves represent the extreme positions of the swaying plume and hence the meandering wave moves with the same periodicity as that of the swaying plume.

Fig. 9 presents time-series averaged velocity and temperature profiles as observed in the centered yz-planes and different planes of xy and xz. As shown in Fig. 9a.1, a distinct U-shaped zone from $z/D = -12$ to -20 in the yz-plane is observed between two closely spaced plumes located at the central location $(x/D = 0)$ in the xy-plane. Additionally, the U-shaped valley in the yz-plane corresponds the plumes swaying outward from the middle of the xy-plane. By comparing the U-shaped zone at different snapshots in Fig. 9a.1 and a.2, this U-shaped region is accordingly observed to translate along the negative z-direction with the same
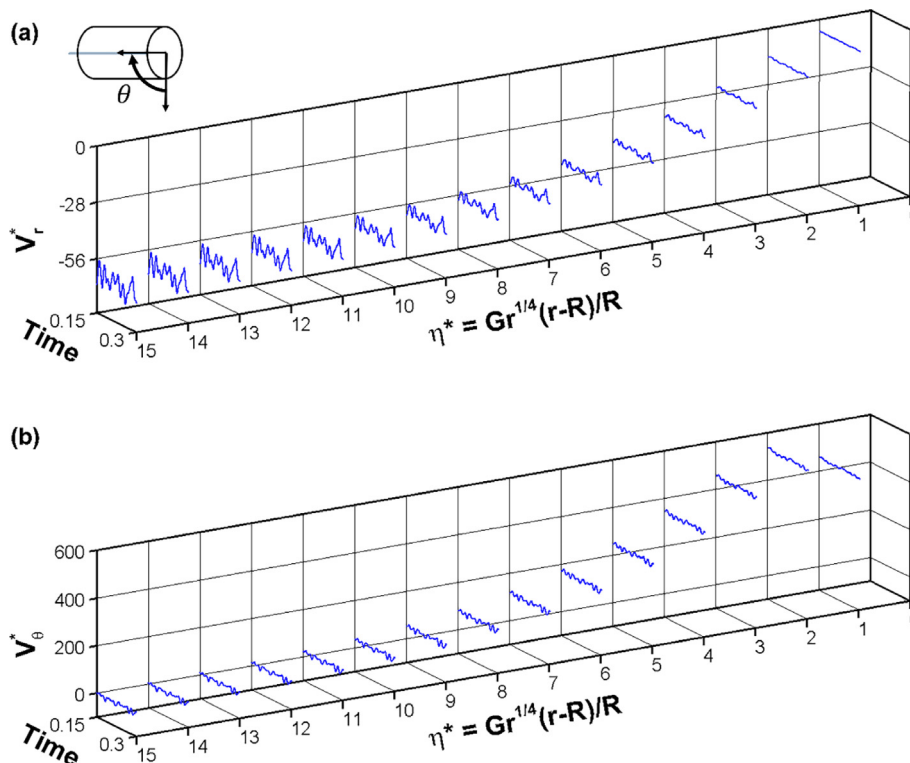

Fig. 5. Dimensionless time histories of radial (V_r^*) (a) and tangential (V_θ^*) (b) velocity profiles along the radial direction. The velocity data are documented at a circumferential location of 90 degrees.
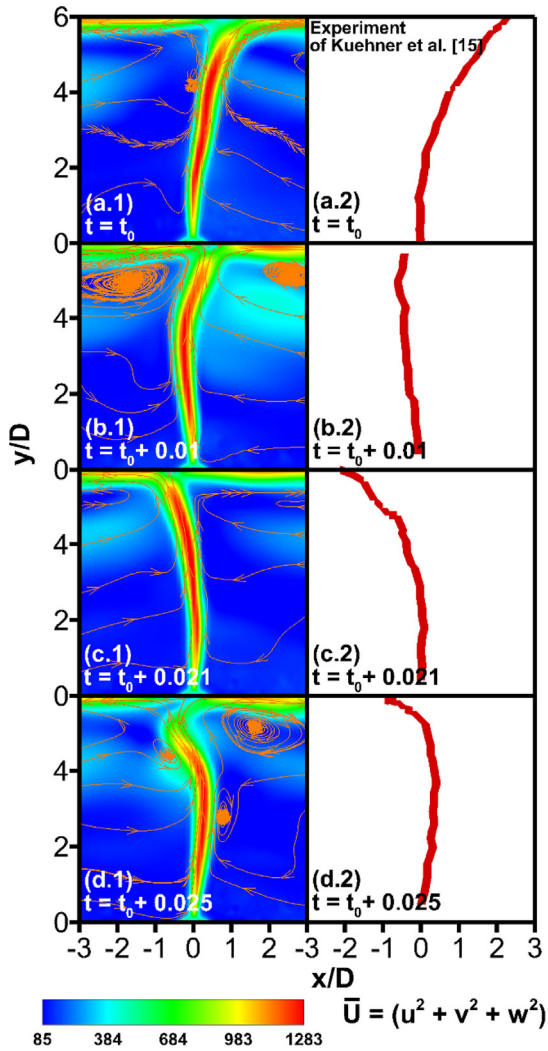
Fig. 6. Mean velocity fields in the *xy*-plane at dimensional time intervals of (a) t'_0, (b) $t'_0 + 0.01$, (c) $t'_0 + 0.021$, (d) $t'_0 + 0.025$: comparison between the numerical simulations and experimentally measured centerlines of the plume from the study of Kuehner et al. [15]. t'_0 is a reference time that corresponds to the start of the plume swaying to the left. $\Delta t = 0.01, 0.021, 0.025$ correspond to the dimensional time of 45 s, 90 s and 110 s, respectively.

periodicity of the travelling sine wave in the *xz*-plane (see Fig. 8). Furthermore, the temperature fields in Fig. 9b.1 and b.2 also form the U-shaped zones corresponding to the velocity snapshots.

A brief analysis for the feedback mechanism as proposed by Kuehner et al. [15] is discussed below. The concave nature of the meandering near free water surface (see Fig. 8a.1 and a.2) pushes the fluid in the plume mixing layer downward to create the penetration depth. However, this relatively warm liquid from the mixing layer permits the buoyancy force that lowers the downward momentum of the fluid. Accordingly, this fluid flow with reduced momentum moves toward the centerline due to the entrainment of the surrounding fluid into the rising fluid, thus giving rise to the cyclic motion vortices seen in the above discussion. It is believed that the movement of vortices along a length of the plume in the *xy*-plane determines swaying directions, periods of swaying plumes and periods of meandering waves. While a mechanism seems to have been established between the meandering structure and swaying, there seems to be no evidence regarding the exact source of these oscillations.
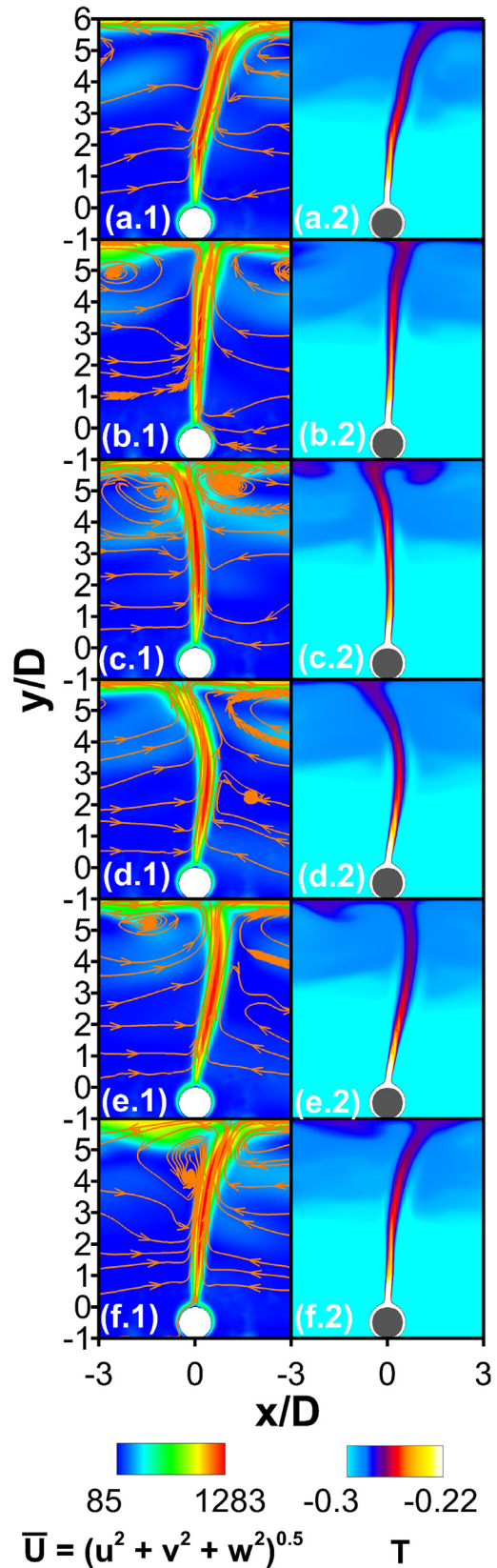

Fig. 7. 2-D central xy-planes of velocity magnitude fields (a) and temperature fields (b) at dimensionless time intervals of (a) t_0, (b) $t_0 + 0.009$, (c) $t_0 + 0.018$, (d) $t_0 + 0.027$, (e) $t_0 + 0.032$ and (f) $t_0 + 0.041$. t_0 is a reference time that corresponds to the start of the plume swaying to the left. The dimensionless swaying period of 0.041 corresponds to 180 s in dimensional time.
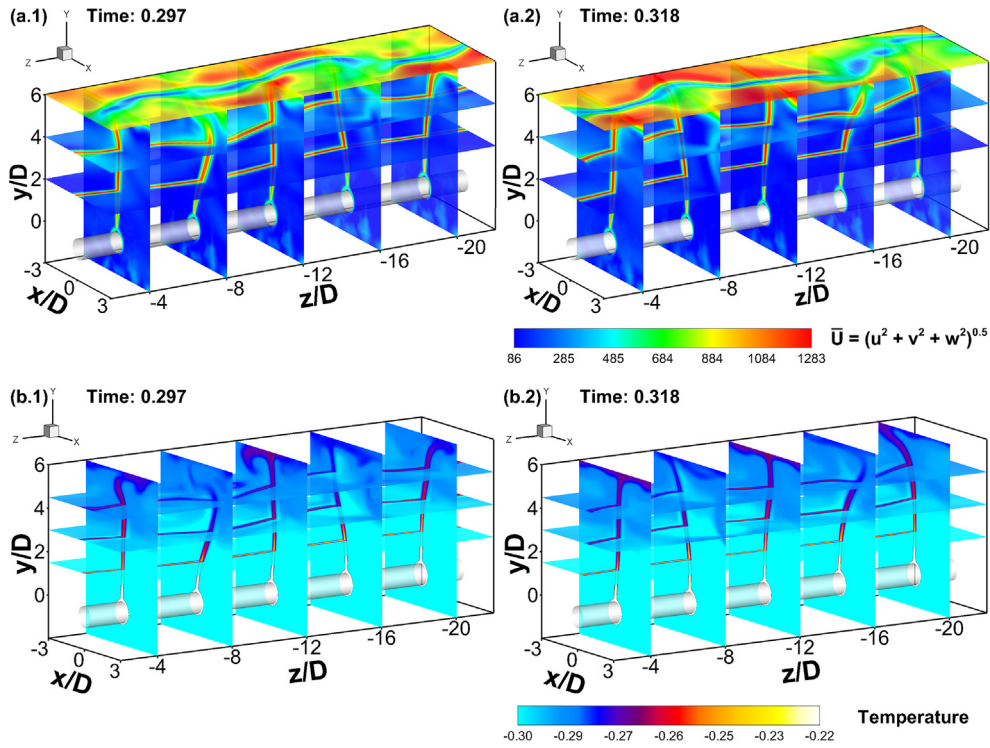
Fig. 8. Variations of mean velocity ($\bar{U}$) and temperature (T) fields in the *xy*- and *xz*-planes. The dimensionless time (t) between fields is 0.021. The time trace starts after the fluid flow reaches the periodically steady state.
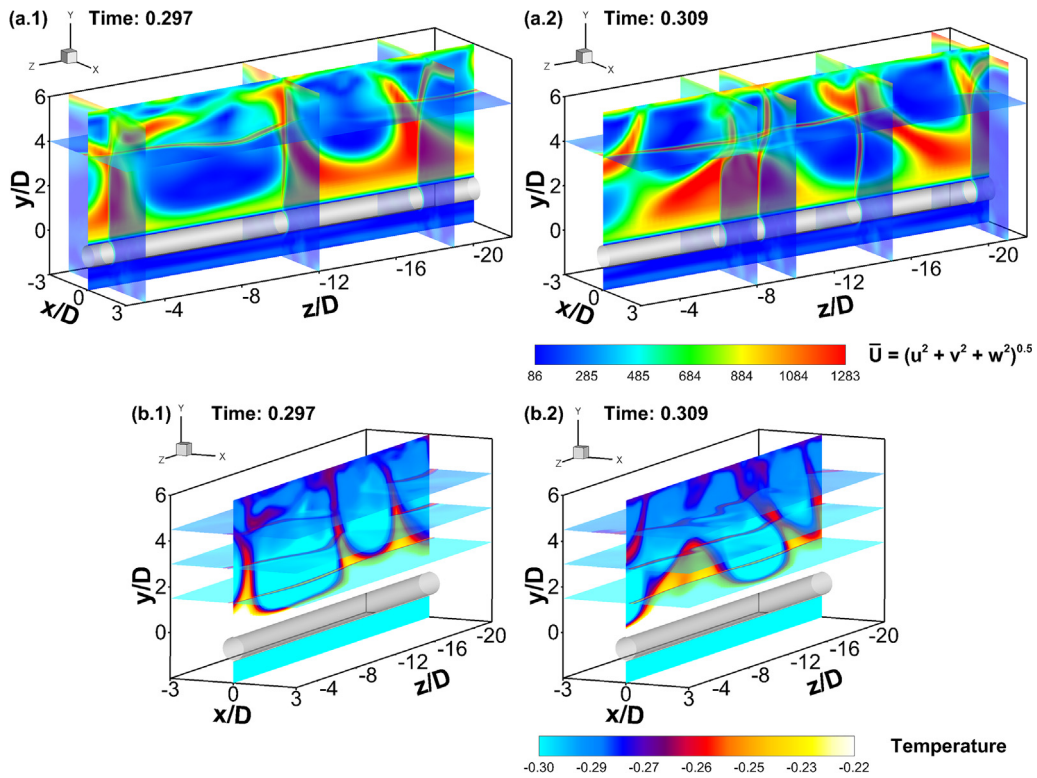

Fig. 9. 3-D mean velocity ($\bar{U}$) and temperature (T) fields with a dimensionless time (t) of 0.012 between the two fields. The time trace starts after the fluid flow reaches the periodically steady state.

3.3. Effect of the Rayleigh number on velocity fields

In this section, the Rayleigh number is varied from 10^5 to 5×10^6, where the buoyancy driven flow around the cylinder is laminar and the heat transfer fluctuations are low [11]. Fig. 10 illustrates the effect of the Rayleigh number on the time-series-averaged radial ($\bar{V}_r^{**}$) and tangential ($\bar{V}_\theta^{**}$) velocity profiles in the

xy-plane. As seen in Fig. 10a, the increased Rayleigh number intensifies the negative $\bar{V}_r^{**}$ values which imply the approach flow moving toward the cylinder at the angular positions of $\theta = 30$–$120°$. At $\theta = 150°$, the time-series-averaged radial velocity ($\bar{V}_r^{**}$) is not much influenced by the change of Rayleigh number in the range 10^5 to 1.33×10^6. At $\theta = 120°$ and $150°$, raising the Rayleigh number from 1.33×10^6 to 5×10^6 drives the flow near $\eta^{**} = 1$–2 going radially outward ($\bar{V}_r^{**} > 0$) from the heated cylinder surface. At $\theta = 180°$, where the fluid flow moves away from the cylinder top toward the plume formation region, the magnitude of the radial velocity ($\bar{V}_r^{**} > 0$) is clearly seen to be proportional to the Rayleigh number. With regard to the variations of the tangential ($\bar{V}_\theta^{**}$) velocity, Fig. 10b shows that the local maximum magnitudes of $\bar{V}_\theta^{**}$ along the boundary-layer radial coordinate (η^{**}) at different angular positions (θ) are pronouncedly influenced by the variation of the Rayleigh number. It is seen in Fig. 10a and b that the strength of natural convection considerably weakens at $Ra = 10^5$ as the profiles of $\bar{V}_r^{**}$ and $\bar{V}_\theta^{**}$ are relatively flat. Nevertheless, we are still able to distinguish the plume structure that slightly meanders above the cylinder top in the temperature contour at $Ra = 10^5$.

Fig. 11 presents the Rayleigh number effect on the local maximum tangential velocity ($\bar{V}_\theta^{**}$) and time-averaged thickness of boundary layers ($\bar{\delta}^{**}$) established in the circumferential range of $30° \leq \theta \leq 150°$. In the Ra range from 10^5 to 1.33×10^6, $\bar{V}_{\theta,max}^{**}$ in Fig. 11a increases upwards along the angular position (θ) and consistently achieves a maximum at $120°$. At $Ra = 5 \times 10^6$, where the strength of heat convection is relatively high, $\bar{V}_{\theta,max}^{**}$ continues to grow at $\theta \geq 120°$ (see Fig. 11a). Furthermore, Fig. 11b shows that the boundary-layer thickness over the cylinder surface is inversely proportional to the Rayleigh number. In particular, the enlargement of the boundary-layer thickness, which is driven by the reduced Rayleigh number, is more pronounced near the plume formation region than on the lower cylinder surface.

3.4. Nusselt number

The variation of ensemble-averaged Nusselt numbers is presented in Fig. 12 for different circumferential positions on the cylinder wall from $\theta = 0°$ to $180°$ at an interval of 30 degrees.
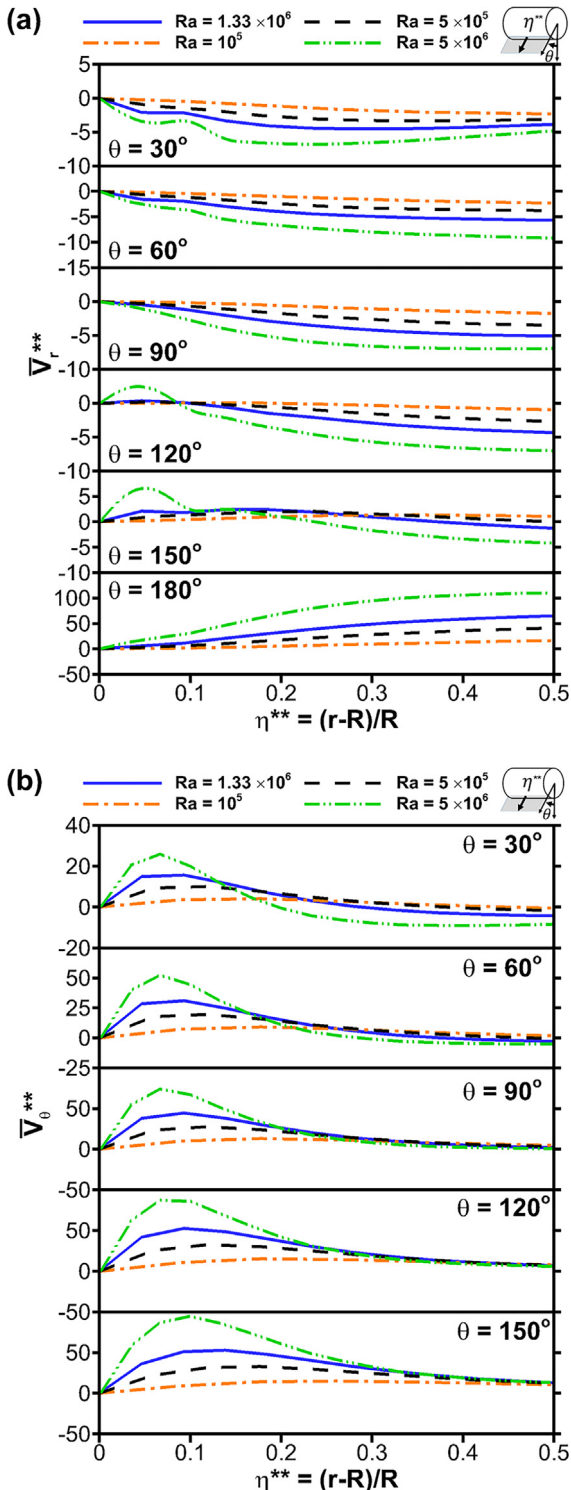

Fig. 10. Time- and z-averaged dimensionless velocities simulated for different Ra numbers in the yz-plan at various circumferential positions (θ) along the radial direction (gray regions): (a) radial ($\bar{V}_r^{**}$) velocity and (b) tangential ($\bar{V}_\theta^{**}$) velocity. The acquisition time of 0.3429 (1500 s) is used.

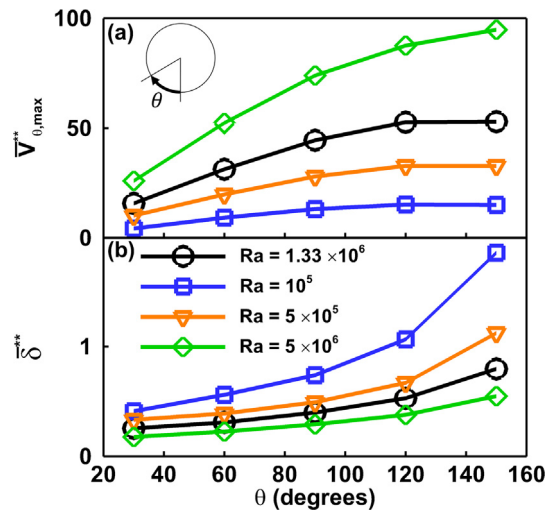**Fig. 11.** Maximum time-averaged tangential velocity ($\bar{V}_\theta^{**}$) (a) and time-averaged boundary-layer thickness ($\bar{\delta}^{**}$) (b) computed for different Rayleigh numbers at various circumferential positions (θ).
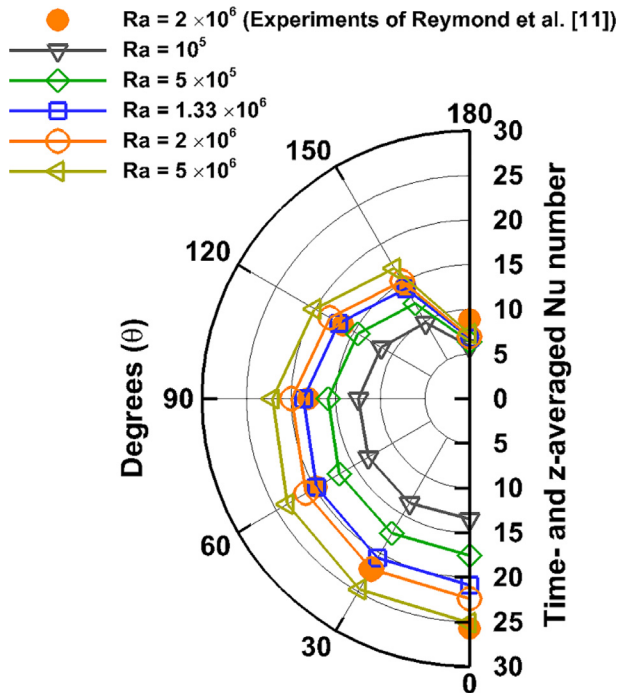
Fig. 12. Variation of the time- and z-averaged Nu number over the circumferential positions (θ) for different Rayleigh numbers.

Fig. 13. Time history of z-averaged Nusselt number at various circumferential positions (θ) for $Ra = 1.33 \times 10^6$. The dimensionless period of 0.23–0.68 corresponds to 1000–3000 s in dimensional time.

Besides, the computational model also accurately predicts the experimentally measured Nu numbers at $Ra = 2 \times 10^6$ reported in the study of Reymond et al. [11]. As expected, the time-series-averaged Nu numbers at $Ra = 1.33 \times 10^6$ are seen to be slightly lower than those at $Ra = 2 \times 10^6$. The Nusselt numbers in Fig. 12 are observed to increase steadily toward the bottom of the cylinder and reach a maximum at $\theta = 0°$. This trend in Fig. 12 corresponds to the variation of flow boundary layer thickness in Fig. 4 along the cylinder surface, where a thin boundary layer increases heat transfer rates. The steep decline of the Nu numbers at $\theta = 180°$ shows relatively poor heat transfer since the rising fluid in the plume shields the top surface of the heated cylinder from the surrounding fluid. As also shown in Fig. 12, the results concerning the enhancement in the Nusselt number by increasing the Rayleigh number indicate that the heat transfer rate gradually expands downwardly from the upper surface.

Fig. 13 shows the temporal variation of the Nu numbers at different circumferential locations for $Ra = 1.33 \times 10^6$ while Table 1 documents the dominant frequencies of the steady-state Nusselt-number oscillations for different Rayleigh numbers determined by the fast Fourier transform (FFT) analysis. Consistent with the experimental findings in the root-mean-square Nu number at $Ra = 2 \times 10^6$ [11], the computed results in Fig. 13 show that the amplitudes at $\theta = 30°$ and $180°$ are slightly greater than those at other circumferential locations. At $\theta = 30°$, where the flow boundary layer is relatively thin, the heat transfer is quite sensitive to the flow pattern and hence the Nu number oscillates significantly. Additionally, the Nu number variation at $\theta = 180°$ is fully dominated by the shedding vortices together with the plume oscillation near the top of the cylinder. Similar to the distribution of the measured root-mean-square Nu numbers at $Ra = 2 \times 10^6$ [11], the computed Nu number variations at $\theta = 60–150°$ are found to be very close. As seen in Table 1, the identified frequency 0.013 Hz at $Ra = 1.33 \times 10^6$ is approximately the same as the half-cycle period of the plume oscillation observed in the experimental study of Kuehner et al. [16]. At $Ra = 1.33 \times 10^6$, the oscillation frequencies of the Nu numbers at $\theta = 30–150°$ are in general at 0.004 Hz (see
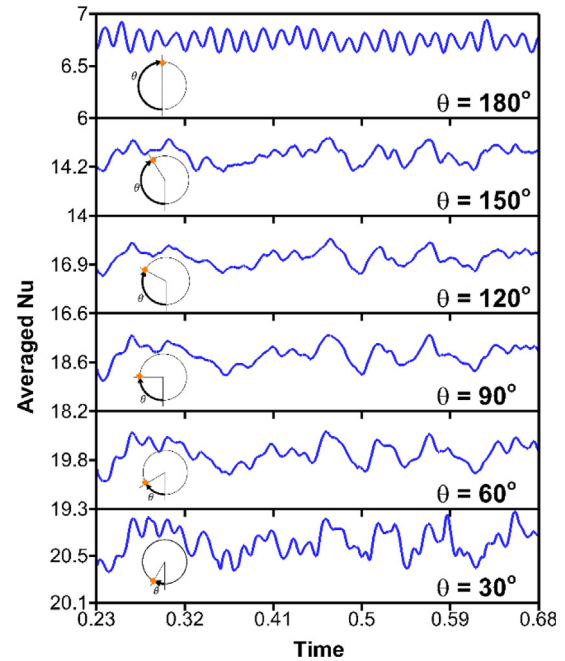
Table 1), which are mostly influenced by the perturbation of the approach flow moving inward to the cylinder.

Generally, the fine spectral resolution is achieved with the dimensionless time period of 0.23 for the various Rayleigh numbers investigated. At $\theta = 180°$, the dominant frequency of Nusselt-number oscillations shown in Table 1 is seen to be proportional to the Rayleigh number. It is worth to note that the presence of multiple discontinuous frequency signals at $Ra = 5 \times 10^6$ implies the possibility of transition from laminar to turbulent flow. At $Ra = 10^5$, the frequency signal in the plume formation region is very low. Besides, the heat transfer frequency with $Ra = 5 \times 10^5$ is particularly greater at $\theta = 180°$ than at other angular positions of $\theta = 30–150°$, a result suggesting that the influence of the plume motion on the lateral and bottom surfaces of the cylinder is not significant.

4. Conclusions

The 3-D natural convection model proposed in this study is the response to the need for understanding complex heat and fluid flow associated with the previous experiments that measured the free convection water flow above a heated horizontal cylinder. The Rayleigh number range from 10^5 to 5×10^6, Prandtl number of 5.98 and normalized submersion depth of $H/D = 6$ are employed. Overall, the simulation well reproduces the experimental PIV measurements at $Ra = 1.33 \times 10^6$, including time-series-averaged radial and circumferential velocities around the cylinder, flow boundary layer thickness, plume swaying motions, plume swaying frequency and temporal variations of fluid flow structures.

The computational results provide us an insight into how the downward penetrative convection affects the boundary-layer thickness and the circumferential position where the boundary layer merges with the plume formation. The plume swaying is observed in the plane perpendicular to the cylinder axis while the plume meandering which behaves like a travelling wave also presents in the other two orthogonal planes. Along the swaying plume, frequent vortex formation and detachment are repeatedly

Table 1
The FFT[a] frequency spectrum (Hz) of the Nusselt-number oscillation with time at various circumferential positions (θ).

θ (°)	Rayleigh number			
	10^5	5×10^5	1.33×10^6	5×10^6
30	0.001–0.002	0.001–0.002	0.004	0.004, 0.011
60	0.003	0.001–0.002	0.004	0.004
90	0.001–0.002	0.001–0.002	0.004	0.004
120	0.001–0.002	0.001–0.002	0.004	0.004
150	0.001–0.002	0.001–0.002	0.004	0.004
180	0.002	0.009–0.01	0.013	0.002, 0.005, 0.015

[a] The time acquisition for the spectral analysis is taken from $t = 0.46$–0.69 corresponding to the dimensional time of 2000–3000 s.

seen in the fluid flow. The temporal variation of the meandering wave and plume swaying in the fluid flow gives an insight into the feedback loop where the downward penetrative convection from the free water surface into rising fluids affects the vortex drifts along the plume motion. The U-shaped velocity profiles in the axial direction are seen to be formed at the timing when plumes cross the U-shaped plane. The effect of Rayleigh number on the radial and tangential velocities is significant. Furthermore, the raised Rayleigh number effectively reduces the thickness of the flow boundary layer and hence increases the heat transfer from the heated cylinder to the fluid.

Also for the first time, an experimentally measured Nu number at $Ra = 2 \times 10^6$ is well predicted by our computational model. In the computational results, we observe that the local Nu number along the cylinder surface increases with the reduction of flow boundary layer thickness. From the FFT analysis of the Nusselt number oscillations, the dominant frequency at the cylinder top is found to be consistent with the half-cycle period of the plume swaying. The frequency of Nusselt number oscillations is seen to be increased with the Rayleigh number. Also, the transition from laminar to turbulent flow may occur at $Ra = 5 \times 10^6$.

Future work is recommended to extend the current investigation to a model with different submersion depths of the cylinder top below the free water surface. This model will aid in examining the effect of the operational conditions on the heat transfer performance.

Acknowledgements

References

[1] A. Schorr, B. Gebhart, An experimental investigation of natural convection wakes above a line heat source, Int. J. Heat Mass Transf. 13 (1970) 557–571.
[2] K. Miyabe, T. Katsuhara, Experimental investigation of the swaying plume above a heated horizontal cylinder, Memoirs of the Kyushu Institute of Technology, Engineering, 1972, pp. 9–22.
[3] L. Pera, B. Gebhart, Experimental observations of wake formation over cylindrical surfaces in natural convection flows, Int. J. Heat Mass Transf. 15 (1972) (175IN5177-5176IN5176).
[4] F. Tetsu, M. Itsuki, U. Haruo, Buoyant plume above a horizontal line heat source, Int. J. Heat Mass Transf. 16 (1973) 755–768.
[5] R. Eichhorn, J. Lienhard, C. Chen, Natural convection from isothermal spheres and cylinders immersed in a stratified fluid, in: Proceedings of 5th International Heat Transfer Conference, 1974, pp. 3–7.
[6] F. Incropera, M. Yaghoubi, Buoyancy driven flows originating from heated cylinders submerged in a finite water layer, Int. J. Heat Mass Transf. 23 (1980) 269–278.
[7] R. Eichhorn, M. Vedhanayagam, The swaying frequency of line source plumes, in: Proceedings of 7th International Heat Transfer Conference, 1982, pp. 407–412.
[8] G. Carlomagno, A. Cenedese, S. Iannetta, LDA velocity measurements in the buoyant plume above a heated horizontal cylinder, Arch. Mech. 36 (1984) 515–521.
[9] K. Kitamura, F. Kami-Iwa, T. Misumi, Heat transfer and fluid flow of natural convection around large horizontal cylinders, Int. J. Heat Mass Transf. 42 (1999) 4093–4106.
[10] M.A. Atmane, V.S. Chan, D.B. Murray, Natural convection around a horizontal heated cylinder: the effects of vertical confinement, Int. J. Heat Mass Transf. 46 (2003) 3661–3672.
[11] O. Reymond, D.B. Murray, T.S. O'Donovan, Natural convection heat transfer from two horizontal cylinders, Exp. Therm. Fluid Sci. 32 (2008) 1702–1709.
[12] S. Grafsrønningen, A. Jensen, B.A.P. Reif, PIV investigation of buoyant plume from natural convection heat transfer above a horizontal heated cylinder, Int. J. Heat Mass Transf. 54 (2011) 4975–4987.
[13] T. Persoons, I.M. O'Gorman, D.B. Donoghue, G. Byrne, D.B. Murray, Natural convection heat transfer and fluid dynamics for a pair of vertically aligned isothermal horizontal cylinders, Int. J. Heat Mass Transf. 54 (2011) 5163–5172.
[14] S. Grafsrønningen, A. Jensen, Natural convection heat transfer from two horizontal cylinders at high Rayleigh numbers, Int. J. Heat Mass Transf. 55 (2012) 5552–5564.
[15] J.P. Kuehner, J.R. Pflug, F.A. Tessier, A.M. Hamed, F.J.M. Marin, Velocity measurements in the free convection flow above a heated horizontal cylinder, Int. J. Heat Mass Transf. 55 (2012) 4711–4723.
[16] J.P. Kuehner, A. Hamed, J.D. Mitchell, Experimental investigation of the free convection velocity boundary layer and plume formation region for a heated horizontal cylinder, Int. J. Heat Mass Transf. 82 (2015) 78–97.
[17] L. Pera, B. Gebhart, On the stability of laminar plumes: some numerical solutions and experiments, Int. J. Heat Mass Transf. 14 (1971) 975–984.
[18] M.-C. Duluc, S. Xin, P. Le Quere, Transient natural convection and conjugate transients around a line heat source, Int. J. Heat Mass Transf. 46 (2003) 341–354.
[19] S.W. Churchill, H.H. Chu, Correlating equations for laminar and turbulent free convection from a horizontal cylinder, Int. J. Heat Mass Transf. 18 (1975) 1049–1053.
[20] V.T. Morgan, The overall convective heat transfer from smooth circular cylinders, Adv. Heat Transf. 11 (1975) 199–264.
[21] M. Muntasser, J. Mulligan, A local nonsimilarity analysis of free convection from a horizontal cylindrical surface, J. Heat Transf. 100 (1978) 165–167.
[22] T. Fujii, Theory of the steady laminar natural convectiol above a horizontal line heat source and a point heat source, Int. J. Heat Mass Transf. 6 (1963) 597–606.
[23] T. Chiang, J. Kaye, On laminar free convection from a horizontal cylinder, in: Proceedings of the 4th National Congress of Applied Mechanics, 1962, pp. 1213.
[24] B. Gebhart, L. Pera, A. Schorr, Steady laminar natural convection plumes above a horizontal line heat source, Int. J. Heat Mass Transf. 13 (1970) (161IN5169-168171).
[25] B. Farouk, S. Güçeri, Natural convection from horizontal cylinders in interacting flow fields, Int. J. Heat Mass Transf. 26 (1983) 231–243.
[26] T.H. Kuehn, R.J. Goldstein, Numerical solution to the Navier-Stokes equations for laminar natural convection about a horizontal isothermal circular cylinder, Int. J. Heat Mass Transf. 23 (1980) 971–979.
[27] T. Saitoh, T. Sajiki, K. Maruhara, Bench mark solutions to natural convection heat transfer problem around a horizontal circular cylinder, Int. J. Heat Mass Transf. 36 (1993) 1251–1259.
[28] P. Wang, R. Kahawita, T. Nguyen, Numerical computation of the natural convection flow about a horizontal cylinder using splines, Numer. Heat Transf. 17 (1990) 191–215.
[29] R. Chouikh, A. Guizani, M. Maalej, A. Belghith, Numerical study of the laminar natural convection flow around an array of two horizontal isothermal cylinders, Int. Commun. Heat Mass Transf. 26 (1999) 329–338.
[30] M. Corcione, Correlating equations for free convection heat transfer from horizontal isothermal cylinders set in a vertical array, Int. J. Heat Mass Transf. 48 (2005) 3660–3673.
[31] C. Cianfrini, M. Corcione, E. Habib, Free convection heat transfer from a horizontal cylinder affected by a downstream parallel cylinder of different diameter, Int. J. Therm. Sci. 45 (2006) 923–931.
[32] M. Corcione, Interactive free convection from a pair of vertical tube-arrays at moderate Rayleigh numbers, Int. J. Heat Mass Transf. 50 (2007) 1061–1074.
[33] M. Corcione, C. Cianfrini, E. Habib, G.M.L. Giudice, Correlating equations for laminar free convection from misaligned horizontal cylinders in interacting flow fields, J. Heat Transf. 130 (2008) 052501.

[34] Q. Pelletier, D.B. Murray, T. Persoons, Unsteady natural convection heat transfer from a pair of vertically aligned horizontal cylinders, Int. J. Heat Mass Transf. 95 (2016) 693–708.

[35] N. Minocha, J.B. Joshi, A.K. Nayak, P.K. Vijayan, 3D CFD simulations to study the effect of inclination of condenser tube on natural convection and thermal stratification in a passive decay heat removal system, Nucl. Eng. Des. 305 (2016) 582–603.

[36] N. Marjang, Calculated surface velocity coefficients for prismatic open channels by three-dimensional hydraulic modeling, in: A Doctoral Dissertation of Utah State University, 2008.

[37] GAMBIT, User's Guide, Ver. 2.3.16, Fluent Inc, 2006.

[38] ANSYS FLUENT 16.1, ANSYS Inc, USA, 2015.